#### **OPEN ACCESS**



# Searching for Intermediate-mass Black Holes in Globular Clusters through Tidal Disruption Events

Vivian L. Tang<sup>1</sup>, Piero Madau<sup>1,2</sup>, Elisa Bortolas<sup>2,3</sup>, Eric W. Peng<sup>4</sup>, Yuting Feng<sup>1</sup>, and Puragra Guhathakurta<sup>1</sup> Department of Astronomy & Astrophysics, University of California, 1156 High Street, Santa Cruz, CA 95064, USA

<sup>2</sup> Dipartimento di Fisica "G. Occhialini," Università degli Studi di Milano-Bicocca, Piazza della Scienza 3, I-20126 Milano, Italy

<sup>3</sup> INFN, Sezione di Milano-Bicocca, Piazza della Scienza 3, I-20126 Milano, Italy

<sup>4</sup> NSF's National Optical-Infrared Astronomy Research Laboratory, 950 North Cherry Avenue, Tucson, AZ 85719, USA

\*\*Received 2023 October 10; revised 2023 December 13; accepted 2024 January 10; published 2024 March 7

#### **Abstract**

Intermediate-mass black holes (IMBHs) may be the link between stellar mass holes and the supermassive variety in the nuclei of galaxies, and globular clusters (GCs) may be one of the most promising environments for their formation. Here, we carry out a pilot study of the observability of tidal disruption events (TDEs) from  $10^3 \, M_\odot < M_\bullet < 10^5 \, M_\odot$  IMBHs embedded in stellar cusps at the center of GCs. We model the long super-Eddington accretion phase and ensuing optical flare, and derive the disruption rate of main-sequence stars as a function of black hole mass and GC properties with the help of a 1D Fokker–Planck approach. The photospheric emission of the adiabatically expanding outflow dominates the observable radiation and peaks in the near-ultraviolet/optical bands, outshining the brightness of the (old) stellar population of GCs in Virgo for a period of months to years. A search for TDE events in a sample of nearly 4000 GCs observed at multiple epochs by the Next Generation Virgo Cluster Survey yields null results. Given our model predictions, this sample is too small to set stringent constraints on the present-day occupation fraction of GCs hosting IMBHs. Naturally, better simulations of the properties of the cluster central stellar distribution, TDE light curves, and rates, together with larger surveys of GCs are all needed to gain deeper insights into the presence of IMBHs in GCs.

Unified Astronomy Thesaurus concepts: Intermediate-mass black holes (816); Globular star clusters (656); Accretion (14)

#### 1. Introduction

There is currently no unambiguous confirmation for intermediate-mass black holes (IMBHs) with masses  $10^2 M_{\odot} \lesssim M_{\bullet} \lesssim 10^5 M_{\odot}$  (for a recent review, see Greene et al. 2020). If one were to extrapolate the known  $M_{\bullet}$ – $\sigma_{\star}$  relation down to low-mass stellar systems, globular clusters (GCs) would be expected to host IMBHs with  $M_{\bullet} \sim 10^3$ – $10^4 M_{\odot}$  (Lützgendorf et al. 2013). Finding objects and characterizing their mass function in this range would provide unique insight into the nature and growth of massive black hole seeds in the early Universe and the dynamical evolution of dense stellar systems, and provide key input into event predictions for gravitational wave facilities. Thus far, there is some circumstantial evidence for black holes below  $10^5 M_{\odot}$  in galaxy nuclei (NGC 205; Nguyen et al. 2019) and in hyperluminous X-ray sources (HLX-1; Webb et al. 2012), but there are still no compelling candidates with  $M_{\bullet} \sim 10^3 M_{\odot}$ .

Different mechanisms have been proposed for the formation of IMBHs in dense stellar clusters, from "slow" scenarios where the black hole remnant of a massive star sinks to the center of the cluster and grows over time through mergers of mass-segregated lighter black holes (Miller & Hamilton 2002), to "fast" collisional runaway of massive stars during an early phase of cluster core collapse, the product of which may eventually lead to the formation of an IMBH (Portegies Zwart & McMillan 2002; Giersz et al. 2015). It has been shown by Miller & Davies (2012) that all clusters above a central velocity dispersion of  $\sigma_{\star} \sim 40 \text{ km s}^{-1}$  will necessarily form an IMBH

Original content from this work may be used under the terms of the Creative Commons Attribution 4.0 licence. Any further distribution of this work must maintain attribution to the author(s) and the title of the work, journal citation and DOI.

through some mechanism at any cosmic epoch, since above this dispersion primordial binaries cannot support the system against deep core collapse. The case is more complicated for lower-dispersion systems such as GCs, where—regardless of how IMBHs form—it may be a challenge to retain them in the face of a repeated onslaught of gravitational wave kicks from mergers with other black holes (Holley-Bockelmann et al. 2008; Fragione et al. 2018a).

To date, there are no solid detections of IMBHs in GCs. Claims of dynamical evidence for IMBHs have been made for multiple clusters, but orbital anisotropies and the presence of high concentrations of dark stellar-mass remnants could account for most or all of the alleged IMBH signatures (see Baumgardt et al. 2019; Zocchi et al. 2019; Vitral & Mamon 2021, and references therein). IMBH detections have been reported by, e.g., Lützgendorf et al. (2013) for NGC 1904 ( $M_{\bullet} = 3000 \pm 1000 \, M_{\odot}$ ) and NGC 6266 ( $M_{\bullet} = 2000 \pm 1000 \, M_{\odot}$ ), Feldmeier et al. (2013) for NGC 5286 ( $M_{\bullet} = 1500 \pm 1000 \, M_{\odot}$ ), Ibata et al. (2009) for NGC 6715 ( $M_{\bullet} \simeq 9$ ,  $400 \, M_{\odot}$ ), and by Kamann et al. (2016) for NGC 6397 ( $M_{\bullet} \simeq 600 \, M_{\odot}$ ). No radio emission consistent with an accreting  $M_{\bullet} \gtrsim 1000 \, M_{\odot}$  IMBH has been observed in a sample of 50 Galactic GCs by Tremou et al. (2018).

To make progress, it is key to develop alternative methods for IMBH searches in dense stellar systems. Tidal disruption events (TDEs) may offer an independent, promising probe. A TDE occurs when the tidal force of the black hole exceeds the star's self-gravity and rips it apart (Rees 1988). While about half of the stellar debris is ejected at high speed, the remainder gets accreted, producing an optical/UV flare accompanied by thermal X-ray emission. One of the most compelling IMBH TDE candidates to date is 3XMM J215022.4–055108 (Lin et al. 2018), an X-ray outburst with a luminosity that peaked at

 $10^{43}\,\mathrm{erg\,s^{-1}}$  and decayed systematically over 10 yr, hosted in a star cluster of mass  $\sim 10^7\,M_\odot$  and plausibly powered by an IMBH of mass  $M_{\bullet}\lesssim 2.2\times 10^4\,M_\odot$  (Wen et al. 2021). This event suggests that an effective means of detecting IMBHs may be through a search of optical flares in a large sample of dense star clusters (e.g., Ramirez-Ruiz & Rosswog 2009; Fragione et al. 2018b; Chen & Shen 2018). As we shall see, this is particularly true for searches in the near-ultraviolet (NUV), where a disruption event is predicted to outshine the old stellar population of the average GC for a period of months to years.

Large surveys with precise multiwavelength photometry are becoming increasingly available for public use. As a pilot experiment, we take advantage of the Next Generation Virgo Cluster Survey (NGVS; Ferrarese et al. 2012), a comprehensive optical imaging survey of the Virgo galaxy cluster, together with its near-infrared counterpart (NGVS-IR; Muñoz et al. 2014), to set constraints on the fraction of GCs that may be harboring IMBHs. The NGVS-IR covers a total area of 4 deg<sup>2</sup> centered on Virgo's core region in the *u grizK*<sub>s</sub> bandpasses, and we capitalize on the sample of nearly 4000 Virgo GCs provided by E. W. Peng et al. (2024, in preparation). We use theoretical optical light curves to search for potential TDE candidates, and the estimated event rates of TDEs for a given GC population, stellar density profile, and cadence of NGVS observations, to attempt to constrain the fraction of GCs hosting IMBHs with stellar cusps at the present epoch. While there are considerable uncertainties in the modeling of TDE events around IMBHs in GCs, we hope that our pilot investigation will provide a blueprint for future searches of optical flares in dense stellar systems.

#### 2. Light Curve Modeling

While the evolution of a TDE light curve has been extensively modeled in the literature (e.g., Strubbe & Quataert 2009; Lodato & Rossi 2011; Strubbe & Quataert 2011; Metzger & Stone 2016; Mockler et al. 2019; Lu & Bonnerot 2020; Ryu et al. 2020, and references therein), the details of the evolution of the debris stream, the efficiency of the process of circularization, and the emission mechanisms responsible for the optical/UV emission in TDE flares all remain an open question (for recent reviews see Roth et al. 2020; Rossi et al. 2021). For illustrative purposes, we shall follow here the simplified analysis of Strubbe & Quataert (2009) and Lodato & Rossi (2011). A star of mass  $M_{\star} = m_{\star} M_{\odot}$  and radius  $R_{\star} = r_{\star} R_{\odot}$  on a very eccentric orbit is torn apart when its pericenter  $r_p$  is within the black hole's tidal sphere of radius

$$r_t = \left(\frac{M_{\bullet}}{M_{\star}}\right)^{1/3} R_{\star}.\tag{1}$$

For lower main-sequence stars, masses and radii are related by  $r_{\star} = m_{\star}^{0.8}$  (Kippenhahn & Weigert 1990). The impact parameter of the encounter,  $\beta = r_t/r_p$ , measures the strength of the tidal interaction. Initially, approximately half of the initial stellar debris becomes bounded (Evans & Kochanek 1989), and after a fallback time,

$$t_{\rm fb} = \frac{\pi}{\sqrt{2}} \left(\frac{r_p}{R_{\star}}\right)^{3/2} \sqrt{\frac{r_p^3}{GM_{\bullet}}},\tag{2}$$

most bound material starts coming back to pericenter at the rate

$$\dot{M}_{\rm fb} = \frac{M_{\star}}{3t_{\rm fb}} \left(\frac{t}{t_{\rm fb}}\right)^{-5/3}.\tag{3}$$

While the early behavior of the fallback rate may be influenced by stellar properties (Lodato et al. 2009; Guillochon & Ramirez-Ruiz 2013; Law-Smith et al. 2020), the late-time accretion rate onto the black hole from a TDE always declines as  $t^{-5/3}$  if the star is completely disrupted (Coughlin & Nixon 2019).

For an IMBH, the mass fallback rate predicted by Equations (2) and (3) exceeds the Eddington rate

$$\dot{M}_E = 10 \frac{4\pi G M_{\bullet}}{C F_{\text{total}}} \tag{4}$$

for a timescale of years or longer. Here,  $\kappa_{\rm es} = 0.34~{\rm cm}^2~{\rm g}^{-1}$  is the electron scattering opacity, and we assume the accretion process at 10% radiative efficiency. In this regime, only a fraction of the fallback material joins the newly formed Keplerian disk and accretes onto the black hole at the rate

$$\dot{M}_{\bullet} = (1 - f_{\text{out}}) \dot{M}_{\text{fb}}, \tag{5}$$

while the remaining stellar debris is launched in a radiation pressure-driven outflow during circularization. The relative importance of accretion and outflows in this phase is poorly understood (e.g., Ohsuga et al. 2005; Dotan & Shaviv 2011; Coughlin & Begelman 2014; Metzger & Stone 2016; Wu et al. 2018). To bracket the uncertainties, here we shall adopt two constant values for the fraction  $f_{\rm out}$  of infalling gas that is ejected in a wind,  $f_{\rm out} = 0.1$  (e.g., Strubbe & Quataert 2009; Kitaki et al. 2021) and  $f_{\rm out} = 0.9$  (e.g., Lodato & Rossi 2011; Metzger & Stone 2016).

The effective temperature of the accretion flow is that of a slim advective disk,

$$\sigma T_d^4(R) = \frac{3GM.\dot{M}.f}{8\pi R^3} \times \left[ \frac{1}{2} + \left\{ \frac{1}{4} + \frac{3}{2} f \left( \frac{10\dot{M}.}{\dot{M}_E} \right)^2 \left( \frac{R_S}{R} \right)^2 \right\}^{1/2} \right]^{-1}$$
 (6)

(Strubbe & Quataert 2009), where  $f \equiv 1 - \sqrt{3R_S/R}$  and  $R_S = 2GM_{\bullet}/c^2$  is the Schwarzschild radius. The disk extends from  $3R_S$  to the circularization radius  $R_c = 2r_p = 2r_t/\beta$ , and the monochromatic disk luminosity as a function of time is that of a multicolor blackbody,

$$L_{\nu} = 4\pi^2 \int_{3R_S}^{R_c} B_{\nu}(T_d) R dR. \tag{7}$$

When required, our standard choice of parameters for the stellar properties is  $\beta=1$ ,  $m_\star=1$ , and  $r_\star=1$ . Figure 1 shows the bolometric light curve for the disk emission from the disruption of a solar-type star by a 3000  $M_\odot$  IMBH. Note how, during the super-Eddington phase, viscosity-generated heat does not have sufficient time to be radiated away, and is instead advected into the hole. The disk effective temperature then remains constant with time even as the fallback rate declines, and the radiated luminosity saturates at a few times  $L_{\rm Edd}$ .

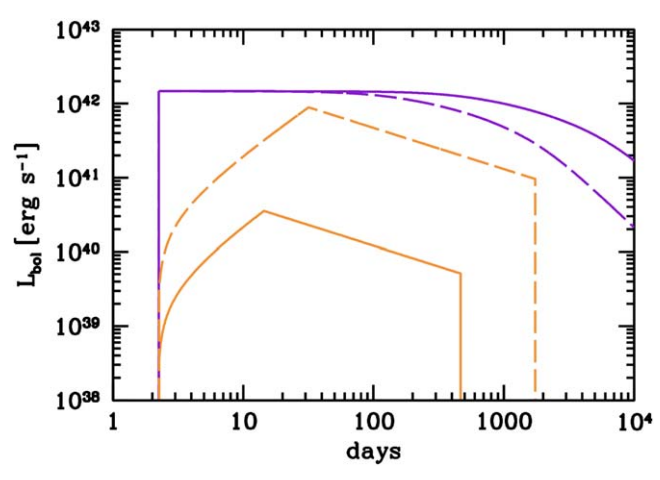


**Figure 1.** Bolometric light curves for the disk (purple lines) and wind (orange lines) emission resulting from the disruption of a solar-type star by a 3000  $M_{\odot}$  IMBH. The time t=0 corresponds to the pericenter passage of the disrupted star, and the fallback time is  $t_{\rm fb}=2.24\,$  days. The solid and dashed lines show, respectively, the  $f_{\rm out}=0.1\,$  and  $f_{\rm out}=0.9\,$  cases for the fraction of infalling gas ejected in the wind (see the main text for details). The  $f_{\rm out}=0.1\,$  outflow becomes optically thin at  $t=469\,$  days.

A simple model for the radiation-driven wind approximates the geometry as spherical and assumes that stellar debris falls back at close to the escape velocity  $v_{\rm esc} = \sqrt{2GM_{\bullet}/R_c}$  and shocks at  $R_c$ , converting kinetic energy into radiation. Photons are trapped in an outflow promptly launched from the circularization radius with  $\dot{M}_{\rm out}(t) = f_{\rm out}\dot{M}_{\rm fb}$  and terminal velocity  $v_w = f_v v_{\rm esc}$ . Our standard choice for the wind velocity parameter is  $f_v = 1$ . The radiation temperature at the base of the wind,  $T_c$ , can be derived from energy conservation in the wind,

$$4\pi R_c^2 v_w(aT_c^4) = \frac{1}{2} \dot{M}_{\text{out}} v_w^2.$$
 (8)

The outer radius of the ejecta grows as  $R_{\rm ej} = R_c + v_w (t-t_{\rm fb})$ , and the outflow is optically thick to electron scattering out to a photospheric radius  $R_{\rm ph}$  given by  $R_{\rm ph} \, \rho_{\rm ph} \, \kappa_{\rm es} = 1$ . The gas density profile for  $r < R_{\rm ej}$  follows from matter conservation,  $\rho(r, t) = \dot{M}_{\rm out}(t)/(4\pi r^2 v_w)$ . The temperature of the advected radiation decreases adiabatically as  $T \propto \rho^{1/3}$ , and photons escape with a blackbody spectrum at the photospheric temperature of

$$T_{\rm ph} = T_c \left(\frac{\rho_{\rm ph}}{\rho_c}\right)^{1/3},\tag{9}$$

where  $\rho_c = \dot{M}_{\rm fb}/(4\pi R_c^2 v_{\rm esc})$  is the gas density at the base of the flow.

At the earliest times, the fallback rate can be so large and the density so high that the location of the photosphere is just inside  $R_{\rm ej}$ . In this "edge-limited" phase, we set  $R_{\rm ph}=R_{\rm ej}$  and  $\rho_{\rm ph}=(R_{\rm ej}~\kappa_{\rm es})^{-1}$ . The specific outflow luminosity is given by

$$L_{\nu} = 4\pi^2 R_{\rm ph}^2 B_{\nu}(T_{\rm ph}). \tag{10}$$

Figure 1 shows the resulting wind bolometric light curve, which rises as  $t^{11/9}$  during the edge-limited initial phase when the photosphere expands and  $T_{\rm ph}$  decreases as  $t^{-7/36}$ . As time passes and the density of the outflow subsides, the photosphere sinks inward as  $t^{-5/3}$ , its temperature rises as  $t^{25/36}$ , and the luminosity declines as  $t^{-5/9}$ . The total radiation luminosity of the wind is of order  $L_{\rm Edd}$  in the  $f_{\rm out}=0.9$  case, decreasing for

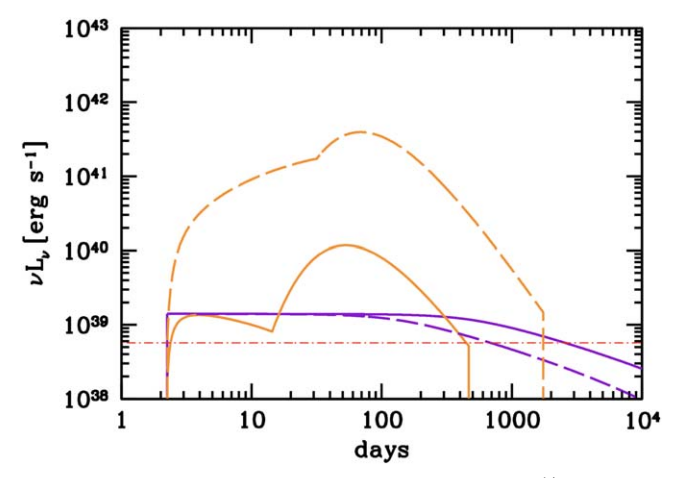


**Figure 2.** Same as Figure 1 but in the u band ( $\nu = 8 \times 10^{14}$  Hz). The red dashed–dotted line shows the mean u-band luminosity,  $\nu L_{\nu} = 5.7 \times 10^{38}$  erg s<sup>-1</sup> of the GCs detected in the NGVS survey (Jordán et al. 2007).

lower outflow rates as  $f_{\rm out}$  during the edge-limited phase, and as  $f_{\rm out}^{5/3}$  afterwards (see Strubbe & Quataert 2009). These relations only apply for  $R_{\rm ph} \geqslant R_c$ , because otherwise, the outflow is optically thin. We impose this limit by setting the wind luminosity to zero when the photosphere shrinks below  $R_c$ . In the  $f_{\rm out}=0.1$  case, the wind becomes optically thin when the fallback rate is still super-Eddington.

While the disk always dominates the total radiated power, the bulk of the disk emission occurs in the soft X-rays. The optical/NUV flash plotted in Figure 2 is instead produced by the adiabatically expanding outflow, which largely outshines the disk during the optically thick phase. For comparison, we also show in the figure the mean NUV luminosity of GCs detected in the NGVS survey, which argues for the detectability of a TDE optical transient against the brightness of a dense star cluster.

Depending on the uncertain geometry of the outflow and the viewing angle of the observer to the source, it is possible that both the accretion disk and the outflow may be visible at early times. Here, we shall neglect obscuration effects and sum up the two contributions to produce a total TDE light curve.

## 3. TDE Rates: Estimates

To provide estimates and trends of the number of TDE flares expected in a local GC survey like the NGVS, we present in this section a simple and intuitive configuration-space approach following Syer & Ulmer (1999). Our treatment is informed by the more rigorous numerical integration of the 1D, orbitaveraged Fokker–Planck equation for the evolution of the stellar distribution function, which we perform and discuss in the next section.

Stars within a cluster of current mass  $M_{\rm GC}$  are assumed to follow a Plummer density profile,

$$\rho_{\star}(r) = \frac{\rho_c}{(1 + r^2/a^2)^{5/2}},\tag{11}$$

with 1D velocity dispersion,

$$\sigma_{\star}^{2}(r) = \frac{\sigma_{c}^{2}}{\sqrt{1 + r^{2}/a^{2}}}.$$
 (12)

Here,  $\rho_c = 3M_{\rm GC}/(4\pi a^3)$  and  $\sigma_c^2 = GM_{\rm GC}/(6a)$  is the density and velocity dispersion in the cluster core, and a is the Plummer scale parameter that sets the size of the cluster core. We have fit the masses and structural parameter data of Milky Way's GCs of Baumgardt & Hilker (2018) with the core density–cluster mass relation:

$$\rho_c = 1.7 \times 10^3 \, \frac{M_{\odot}}{\text{pc}^3} \left( \frac{M_{\text{GC}}}{10^5 \, M_{\odot}} \right)^2. \tag{13}$$

For a GC with mass  $M_{\rm GC} = 5 \times 10^5 \, M_{\odot}$ , the expressions above yield  $\rho_c = 4.3 \times 10^4 \, M_{\odot} \, {\rm pc}^{-3}$ ,  $a = 1.4 \, {\rm pc}$ , and  $\sigma_c = 16 \, {\rm km \, s}^{-1}$ .

At the center of this Plummer cluster, we place an IMBH with  $M_{\bullet} \ll M_{\rm GC}$ . Following mass segregation (Bahcall & Wolf 1977), low-mass main-sequence stars and their remnants relax to a Bahcall-Wolf  $r^{-\gamma}$  density cusp near the black hole, with  $3/2 < \gamma < 7/4$  (Alexander & Hopman 2009). We thus write the stellar density near the center of the cluster as

$$\rho_{+}(r) = \rho_{c} \left[ 1 + (R_{i}/r)^{\gamma} \right],$$
 (14)

where  $R_i \ll a$  is the radius of influence of the black hole. This is defined as the location where the interior stellar mass equals  $M_{\bullet}$  (e.g., Binney & Tremaine 1987; Merritt 2004; Wang & Merritt 2004), i.e.,

$$R_i \equiv \left[ g(\gamma) \frac{M_{\bullet}}{M_{\rm GC}} \right]^{1/3} a, \tag{15}$$

where  $g(\gamma) = (3 - \gamma)/(6 - \gamma)$ . In our set-up,  $R_i$  is typically a few times larger than the radius  $r_* \equiv GM_*/\sigma_c^2$  defined kinematically in terms of the intrinsic stellar velocity dispersion. For IMBHs weighing a few percent of the cluster core mass, collisional N-body simulations show that the  $\rho_* \propto r^{-\gamma}$  cusp extends all the way up to  $R_i > r_*$  (Baumgardt et al. 2004). This is also confirmed in our direct numerical integration of the Fokker–Planck equation for the time-dependent stellar distribution in the vicinity of an IMBH (see Section 4). The Jeans equations associate an  $r^{-\gamma}$  density cusp with a velocity dispersion that near the black hole approaches  $\sigma_*^2 \to GM_*/[(1 + \gamma)r]$  (e.g., Zhao 1996). We therefore approximate the cluster central velocity dispersion as

$$\sigma_{\star}^{2}(r) = \sigma_{c}^{2} + \frac{GM_{\bullet}}{(1+\gamma)r}.$$
 (16)

Hereafter, we shall assume a slope of  $\gamma = 7/4$  for the central stellar cusp.

Stars on nearly parabolic orbits are tidally disrupted when their specific angular momentum J is smaller than  $J_{\rm lc} = (2GM \cdot r_{\rm l})^{1/2}$ . The ensemble of nearly radial orbits with  $J < J_{\rm lc}$  forms the so-called "loss cone," the set of velocity vectors at some distance r from the black hole that lie within a cone of half-angle  $\theta_{\rm lc}$  (Frank & Rees 1976; Lightman & Shapiro 1977),

$$\theta_{\rm lc}^2 = \frac{GM \cdot r_t}{\sigma^2 r^2}.$$
 (17)

Stars in the loss cone are disrupted at the first periapsis passage, and the continued supply of stars to the IMBH is driven by gravitational deflections that repopulate the loss cone on a timescale that is related to the two-body relaxation time,

$$t_R = \frac{0.34 \,\sigma_\star^3}{G^2 \langle M_\star^2 \rangle n_\star \ln \Lambda} \tag{18}$$

(Spitzer 1987). Here,  $n_{\star} = \rho_{\star}/\langle M_{\star} \rangle$  is the number density of main-sequence stars and their remnants, and we take  $\ln \Lambda = \ln(0.4 \, M_{\star}/\langle M_{\star} \rangle)$  for the Coulomb logarithm. In a simplified treatment, two dynamical regimes can be defined depending on the ratio of the dynamical timescale,  $t_d = r/\sigma_{\star}$ , to the diffusion timescale of angular momentum across the loss cone,  $t_{\rm lc} = \theta_{\rm lc}^2 t_R$ . Close to the IMBH, orbital periods are short and stars diffusing into the loss cone are immediately disrupted. This is the empty loss-cone regime, and the rate of TDEs per star can be estimated as

$$\frac{d\dot{N}_{<}}{dN_{\rm MS}} = \frac{1}{\ln(2/\theta_{\rm lc})t_R},\tag{19}$$

where  $N_{\rm MS}(< r)$  is the number of main-sequence stars contained within a radius r (Frank & Rees 1976; Lightman & Shapiro 1977; Syer & Ulmer 1999). This flux is proportional to the relaxation rate but only weakly dependent on the size of the loss cone. In the other regime,  $t_d > t_{\rm lc}$ , scattering in and out of the loss cone is faster than the orbital time, and the loss cone will always be full and uniformly populated in the orbital phase. The fraction of stars in the loss cone at any time is then just  $\theta_{\rm Ic}^2$ , and the TDE rate per star is given by Syer & Ulmer (1999),

$$\frac{d\dot{N}_{>}}{dN_{\rm MS}} = \frac{\theta_{\rm lc}^2}{t_d},\tag{20}$$

independent of the stellar encounter timescale. After solving for the transition radius  $r_{\rm crit}$ , where the two per-star disruption rates in Equations (19) and (20) are equal, we write the total TDE rate of main-sequence stars as

$$\dot{N}_{\text{TDE}} = \dot{N}_{<} + \dot{N}_{>} = 4\pi \int_{0}^{r_{\text{crit}}} \frac{n_{\text{MS}} r^{2}}{\ln(2/\theta_{\text{lc}}) t_{R}} dr + 4\pi \int_{r_{\text{crit}}}^{\infty} \frac{n_{\text{MS}} GM \cdot r_{t}}{\sigma_{\star} r} dr.$$
(21)

In the above equations, the term  $\langle M_{\star} \rangle$  represents the change in the event rate with the number of stars at fixed total stellar density  $\rho_{\star}$ , while the second moment  $\langle M_{\star}^2 \rangle$  is responsible for the decrease of the diffusion timescale as the gravitational potential becomes more "granular" and stellar-mass black holes dominate the relaxation rates (Kochanek 2016; Bortolas 2022). In general, to compute  $\langle M_{\star} \rangle$  and  $\langle M_{\star}^2 \rangle$  one needs to adopt a present-day mass function (PDMF) with an upper truncation at  $M_{\star}^{\rm max} \approx 1 \, M_{\odot}$  to approximate the old stellar population of a GC (Magorrian & Tremaine 1999). For simplicity, and in analogy with the time-dependent Fokker-Planck numerical approach discussed in the next section, we will assume instead an idealized, single-mass stellar system composed of  $M_{\star} = 1 M_{\odot}$ stars  $(n_{\rm MS}=n_{\star})$ . Compared to a single-mass stellar population, a realistic PDMF is known to enhance TDE rates by several-fold (Stone & Metzger 2016) even after accounting for the smaller tidal radii,  $r_t \propto M_{\star}^{-1/3} R_{\star} \propto M_{\star}^{7/15}$ , of subsolar stars.<sup>5</sup>

Figure 3 shows the predicted TDE rates for  $10^3 < M_{\bullet}/M_{\odot} < 10^4$  IMBHs in GCs with a single-mass stellar population and

 $<sup>\</sup>overline{^5}$  In our model, the empty loss-cone disruption rate can be shown to scale as  $\dot{N}_{<} \propto r_t^{4/9}$  up to a slowly varying logarithmic factor.

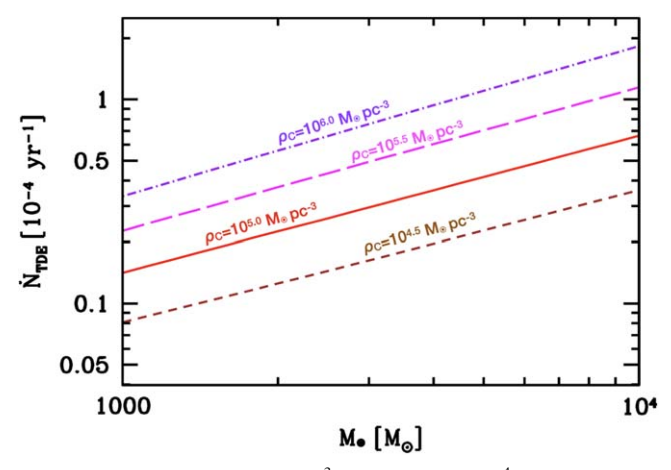


**Figure 3.** Predicted TDE rates for  $10^3\,M_\odot < M_\bullet/M_\odot < 10^4$  IMBHs embedded in  $r^{-7/4}$  stellar cusps at the center of GCs with  $\rho_c = 10^{4.5}\,M_\odot$  pc<sup>-3</sup> (short dashed curve),  $10^{5.0}\,M_\odot$  pc<sup>-3</sup> (solid curve),  $10^{5.5}\,M_\odot$  pc<sup>-3</sup> (long dashed curve), and  $10^{6.0}\,M_\odot$  pc<sup>-3</sup> (dotted–dashed curve). Both the empty and full loss-cone regimes contribute an  $\mathcal{O}(1)$  fraction of the total TDE rate. These calculations assume a single-mass stellar system composed of  $M_\star = 1\,M_\odot$  stars.

increasing core densities in the range  $\rho_c = 10^{4.5} - 10^6 \, M_\odot$  pc $^{-3}$ . Most events are sourced at  $r_{\rm crit} < R_i$ , and both the empty and full loss-cone regimes contribute an  $\mathcal{O}(1)$  fraction of the total disruption rate. The rates of TDEs increase with black hole mass and cluster core density approximately as  $\dot{N}_{\rm TDE} \sim (\rho_c M_\bullet)^{0.5}$ , and typically exceed  $10^{-5} \, {\rm yr}^{-1}$  for  $\gtrsim 10^3 \, M_\odot$  IMBHs harbored in dense GCs. Obviously, these high rates cannot be sustained indefinitely because of stellar depletion. In the next section, we will compute TDE rates in a time-evolving stellar density profile—including depletion—using a Fokker–Planck approach.

## 4. TDE Rates: Fokker-Planck Integration

We have tested the simplified model of the previous section against the results of the PHASEFLOW Fokker-Planck integrator of Vasiliev (2017). The publicly available PHASEFLOW code solves the coupled Poisson and orbit-averaged 1D Fokker-Planck equations, evolving a spherically symmetric distribution of stars under two-body relaxation and loss-cone effects in the neighborhood of a central black hole, the mass of which is allowed to grow with time following stellar captures (Bortolas 2022). We explore a one-parameter family of models, varying the initial core density of the initial Plummer profile between  $10^{4.5}$  and  $10^6\,M_\odot\,{\rm pc}^{-3}$  and adjusting the total mass of the cluster according to Equation (13)  $(M_{\rm GC} = 4.3 \times 10^5 - 2.4 \times 10^6 \, M_{\odot})$ . In all configurations, a central IMBH of initial mass  $M_{\bullet}(t=0) = 600 M_{\odot}$  is embedded in an  $r^{-7/4}$  initial stellar cusp that extends all the way up to the influence radius  $R_i$ . Following each capture event, 30% of the mass of the disrupted star is accreted by the IMBH. For simplicity, we assume here an idealized, single-mass stellar system composed of  $M_{\star} = 1 M_{\odot}$  stars, postponing a numerical treatment that includes a complete, time-dependent stellar mass function and the effect of mass segregation on TDE rates to future work.

Figure 4 shows the evolving stellar density profiles of four IMBH+GC systems with different initial core densities in the range  $\rho_c = 10^{4.5}$ – $10^6 \, M_\odot$  pc<sup>-3</sup> (as in Figure 3). As shown by Vasiliev (2017), the cusp is not a steady-state structure: the gray line shows the initial Plummer+Bahcall-Wolf cusp profile (t = 0), the red line corresponds to the time when the cusp amplitude attains its maximum value, and the blue line depicts the profile at the end of the integration, t = 14 Gyr, when the cusp density

normalization has decreased in response to the heat source at the center. In the figure, the vertical lines mark the influence radius  $R_i$  containing a mass of stars equal to  $M_{\bullet}(t)$ , while the starred points denote the locus where most TDEs are sourced.

The evolution of all clusters follows a similar route. At first the system expands, powered by an outward heat conductive flux driven by two-body relaxation. The density in the cusp decreases, roughly maintaining an  $r^{-7/4}$  profile inside the influence radius. The initial expansion phase lasts  $\sim 0.1$  Gyr, which is of order the two-body relaxation timescale at the influence radius  $R_i(t=0)$ , and is followed by a phase of secular gravothermal contraction leading to a maximum cusp density at time  $t_{\rm peak} \simeq 8$  Gyr; as expected, the latter timescale is of order the relaxation timescale measured in the outer regions of the cluster. IMBH–star interactions eventually generate enough heat to prevent further core collapse and cause a late re-expansion of the cluster.

During the 14 Gyr evolution, the IMBH acquires a mass of 2919–48,720  $M_{\odot}$  depending on the chosen initial stellar density, with a more efficient growth in the case of denser and more massive systems (Figure 5) and a faster rise at time t = 7-9 Gyr during the gravothermal cluster contraction. The three main phases of the GC density profile progression—fast expansion, contraction of the core, and slow re-expansion-are reflected in the evolution of the TDE rate (Figure 6), which is simultaneously modulated by the growth of the central black hole. Disruption rates reach a minimum after 0.1-0.2 Gyr, then climb dramatically by more than 2 orders of magnitude during core contraction, peak at  $t_{\rm peak} \simeq 8$  Gyr, and slowly decay at late times. The peak in the rates is clearly sourced by the collapse of the outer regions of the cluster delivering a substantial amount of new stars near the IMBH and promoting its growth. Peak rates are more pronounced in initially denser clusters where stellar captures lead to more massive IMBHs. The orbital radius where most disruption events originate (starred point in Figure 4) moves outward during the core expansion phases, and inward when the core contracts.

Because of the intrinsic time dependence of the problem, a detailed comparison between our steady-state analytical estimates in Section 3 and the numerical results obtained with the PHASEFLOW code is far from trivial. The Fokker–Planck integration validates qualitatively:

- 1. The assumed steady-state inner density profile, which actually evolves in amplitude in Figure 4 but approximately retains the same  $r^{-7/4}$  functional form, with little dependence on initial conditions.
- 2. The IMBH mass range used to estimate light curves and TDE rates in GCs, which is consistent with the mass accreted in ∼7–8 Gyr by sufficiently massive black hole seeds (with seed masses above a few hundred solar masses) via stellar captures in dense stellar systems (see Figure 5).
- 3. The trends of increasing TDE rates with  $M_{\bullet}$  and  $\rho_c$  (Figure 3), which are also seen in our numerical integration model (Figure 6).

When compared with our steady-state analytical estimates for a single-mass stellar population of  $1\,M_\odot$  stars (Figure 3), the peak rates observed in the Fokker-Planck integration appear to be a few times lower than the corresponding rates of the simplified model.

In our analysis below of the NGVS GC sample, we shall adopt for simplicity the analytical rates of Figure 3, as they are expected to be intermediate between the numerical results and steady-state estimates that include a complete, evolved stellar

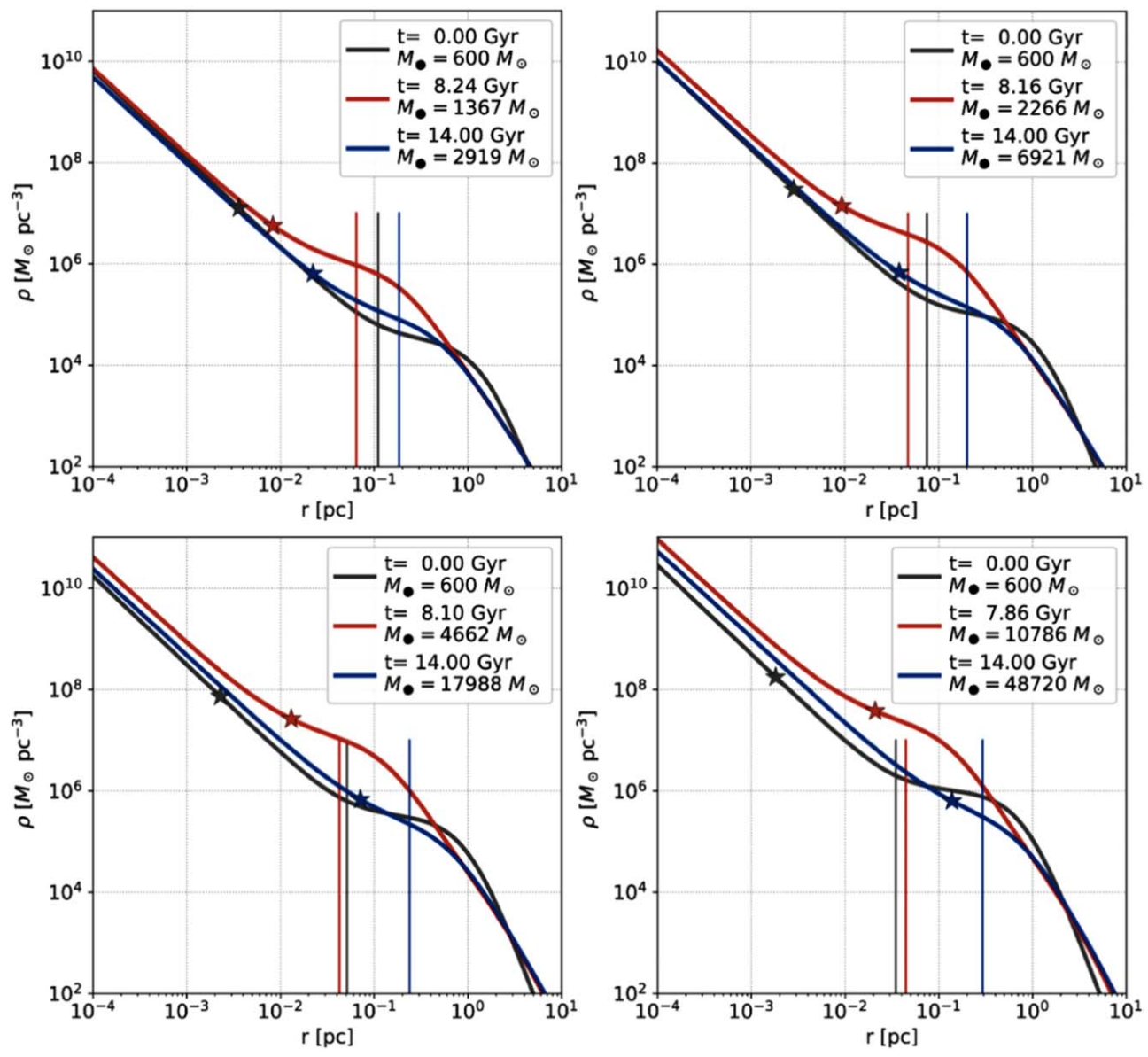


Figure 4. Evolution of the stellar density profile of four IMBH+GC systems with initial Plummer core densities  $\rho_c = 10^{4.5} \, M_\odot \, {\rm pc}^{-3}$  (top left panel),  $10^{5.0} \, M_\odot \, {\rm pc}^{-3}$  (top left panel),  $10^{5.0} \, M_\odot \, {\rm pc}^{-3}$  (top left panel), and  $10^{6.0} \, M_\odot \, {\rm pc}^{-3}$  (bottom right panel). In all cases, a central IMBH of initial mass  $M_\bullet(t=0) = 600 \, M_\odot$  is embedded in a preexisting  $r^{-7/4}$  stellar cusp that extends all the way up to the influence radius (vertical lines in the panels). The starred points denote the locus where most TDEs are sourced. The collisional evolution of these spherical isotropic stellar systems under two-body relaxation and loss-cone effects was simulated by integrating the coupled Poisson and orbit-averaged 1D Fokker–Planck equations with the code PHASEFLOW (Vasiliev 2017) for a single-mass stellar system composed by  $M_\star = 1 \, M_\odot$  stars.

mass function. A useful power-law fit to these TDE rates as a function of  $M_{\bullet}$  and  $\rho_c$  is given by

$$\dot{N}_{\text{TDE}} = a \left( \frac{\rho_c}{M_{\odot} \text{ pc}^{-3}} \right)^b \left( \frac{M_{\bullet}}{10^5 M_{\odot}} \right)^c, \tag{22}$$

with parameters  $a = (2.2 \pm 0.3) \times 10^{-6} \text{ yr}^{-1}$ ,  $b = 0.44 \pm 0.002$ , and  $c = 0.71 \pm 0.005$ .

## 5. NGVS GC Sample

To compare our theoretical predictions with observations, we search for optical flares from TDEs in a robust sample of GCs in the *u* and *g* bands. These clusters are in the core of the nearby Virgo galaxy cluster within a 2 deg<sup>2</sup> region centered on M87. The photometric data are part of the NGVS (Ferrarese et al. 2012) and its near-infrared counterpart, NGVS-IR (Muñoz et al. 2014). GC candidates were selected using extreme deconvolution (Bovy et al. 2011) to model the distribution of foreground stars, GCs, and background galaxies in a multidimensional parameter space of color and morphology (concentration parameter), which determined the probability of a given source to be a GC (E. W. Peng et al. 2024, in preparation). Our sample of NGVS GC consists of CFHT MegaCam time-series photometry in the *ugiz* bandpasses spanning 5 yr with a cadence timescale ranging from hours to

<sup>&</sup>lt;sup>6</sup> Note that such an event rate cannot be sustained indefinitely, as nearly the entire cluster would be consumed over a Hubble time. The time evolution in Figure 6 shows that high rates are only achieved at late times. Considering that most GCs are about 10 Gyr old, i.e., they are close in age to the peak of the TDE rate in the figure, it is reasonable to use this value as a good estimate for the present-day TDE rate.

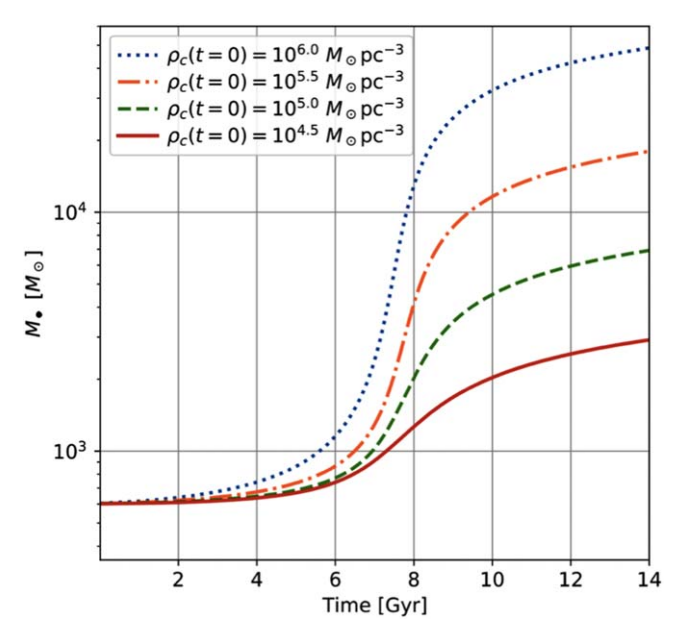


**Figure 5.** The growth of central IMBHs by stellar captures in the time-evolving stellar density profiles of Figure 4. In all configurations, the initial black hole mass was fixed to  $M_{\bullet}(t=0) = 600~M_{\odot}$ . Plummer core initial densities range from  $\rho_c(t=0) = 10^{4.5}~M_{\odot}~{\rm pc}^{-3}$  (solid line) at the bottom to  $10^{6.0}~M_{\odot}~{\rm pc}^{-3}$  (dotted line) at the top.

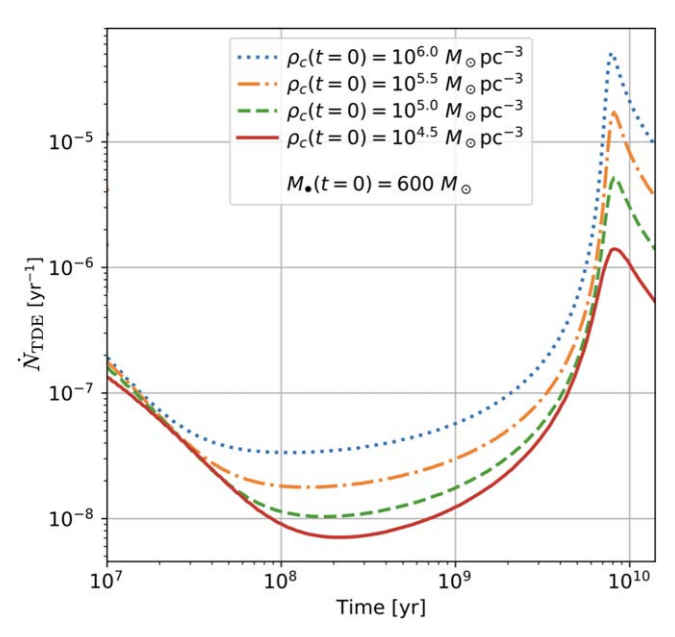


**Figure 6.** Predicted TDE rates in the time-evolving stellar density profiles of Figure 4. A single-mass stellar system composed of  $M_{\star} = 1 \, M_{\odot}$  stars was assumed for simplicity in the numerical integration of the coupled Poisson and orbit-averaged 1D Fokker–Planck equations with PHASEFLOW. In all cases, a central IMBH of initial mass  $M_{\bullet}(t=0) = 600 \, M_{\odot}$  was embedded in a preexisting  $r^{-7/4}$  stellar cusp (see the main text for details).

months and sometimes several years. The cadence was determined by the need to make large dithers for studying the low surface brightness outskirts of massive galaxies (Ferrarese et al. 2012). Most GCs have about 5–20 measurements in each of the four filters with 0.05–0.2 mag photometric precision depending on the apparent magnitude of the system. After removing those with only single-epoch observations, our final NGVS sample of GCs with *u*-band photometry includes a total of 3849 sources.

## 5.1. Photometric Variability

A temporary brightening of an NGVS GC could indicate a potential TDE, a false positive due to cosmic-ray hits, or other image artifacts. We have checked for large photometric variations, applying a sigma-clipping technique to find outliers in subsets of data. Four outliers at  $3.5\sigma$  were found in the u band, and image inspection showed that cosmic rays were causing the increase in brightness. Our search for detectable TDE events in the NGVS GC sample yields null results.

#### 5.2. Mass and Luminosities

Stellar masses of NGVS GCs were computed from their AB magnitudes  $m_{AB}$  as

$$m_{\rm AB} = C - 2.5 \log M_{\rm GC}.$$
 (23)

The constant C includes the logarithm of a mass-to-light ratio  $\Upsilon$  in any arbitrary bandpass and the distance d to the Virgo cluster [16.5  $\pm$ 0.1 (random)  $\pm$ 1.1 (systematic) Mpc; Mei et al. 2007], and is given by

$$C = M_{\odot} + 2.5 \log \Upsilon + 5 \log \left(\frac{d}{10}\right).$$
 (24)

From the reported MegaCam photometry, we take the average g- and z-band magnitudes and compute for each GC the color  $(\overline{g} - \overline{z})$ . The colors are then used to obtain z-band mass-to-light ratios by adopting the corresponding values predicted by the metallicity-dependent population-synthesis model PEGASE (Jordán et al. 2007). The resulting NGVS GC mass distribution is shown in Figure 7. The GC sample has mean stellar mass  $\langle M_{GC} \rangle = 1.1 \times 10^6 \, M_\odot$ , and 31% of all GCs are more massive than  $10^6 \, M_\odot$ . We used the z band rather than the g band for mass determinations because mass-to-light ratios at redder wavelengths are less sensitive to the exact age or star formation history of a stellar population, minimizing systematic uncertainties. Figure 7 also shows the u- and g-band monochromatic luminosities of our GC sample. Globulars are typically fainter in u, with NUV luminosities rarely exceeding  $10^{39} \, \mathrm{erg \, s}^{-1}$ .

## 5.3. Detectability of TDEs in NGVS GCs

To assess quantitatively the observability of TDEs in our GC sample, and in preparation for future multiepoch surveys of extragalactic star clusters, we assume here that each NGVS GC hosts an IMBH of mass  $0.01\,M_{\rm GC}$ . The input parameters for each cluster are its stellar luminosity, the corresponding TDE rate (Equation (22)), and the theoretical light curves in the two cases,  $f_{\rm out}=0.1$  and  $f_{\rm out}=0.9$ , chosen to bracket the strength of the radiation-driven wind component. For each GC we then compute the time interval  $\Delta t_{\rm TDE}$  during which the TDE outshines the steady stellar GC component in the u band, as well as the total time span between the first and last epoch of cluster observation,  $\Delta t_{\rm S}$ . The number of observable TDEs in the sample is then

$$N_{\text{TDE}} = f_{\text{occ}} \sum_{i} \dot{N}_{\text{TDE},i} (\Delta t_{\text{TDE},i} + \Delta t_{S,i}). \tag{25}$$

Here, the sum is over all GCs,  $f_{\rm occ}$  < 1 is the occupation fraction, and the first term on the right-hand side corrects for the events that went off before the start of the survey but whose

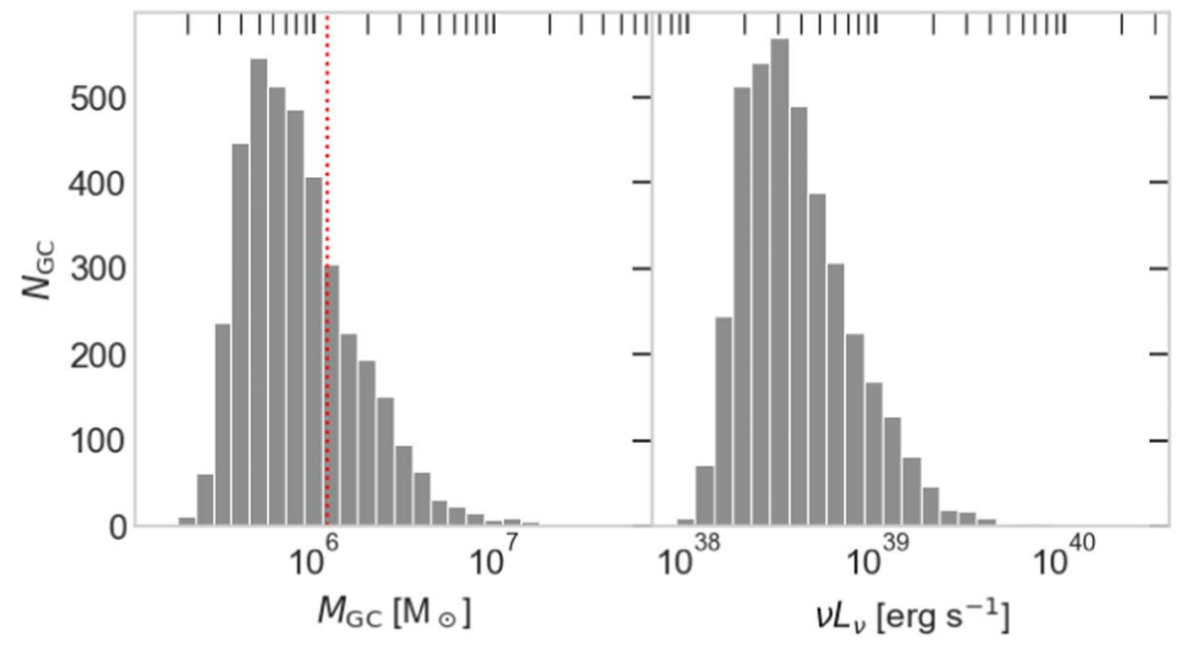


Figure 7. Stellar mass (left panel) and mean monochromatic luminosity (right panel) distributions of NGVS GCs. Stellar masses are computed using the *z*-band mass-to-light ratios predicted by the metallicity-dependent population-synthesis model PEGASE (Jordán et al. 2007). The vertical red dashed line marks the mean value of the distribution,  $\langle M_{\rm GC} \rangle = 1.1 \times 10^6 \, M_{\odot}$ . In the *u* band, most GCs are fainter than  $10^{39}$  erg s<sup>-1</sup>.

light-curve tail would still be visible at survey times. Note that typically  $\Delta t_{\text{TDE}} > \Delta t_S$ , and that  $\Delta t_S$  can be as long as 5.1 yr.

Our model predicts  $N_{\text{TDE}}/f_{\text{occ}} = (10, 4)$  events for  $f_{\text{out}} = (0.1, 0.9)$ , respectively. Monte Carlo simulations of TDEs occurring randomly at the rate  $N_{\text{TDE},i}$  and observed for a timescale  $\Delta t_S$  at the cadence of the NGVS confirm these basic estimates. Figure 8 shows the distribution of  $\Delta t_{\text{TDE}}$  for our GC sample at varying  $f_{\text{out}}$ , with the weaker winds+disk systems outshining the steady stellar component for longer timescales because of late time accretion. Figure 9 shows three examples of TDE mock detections in the Monte Carlo simulations, with the TDE light curve (the sum of the disk and wind components) compared to the steady stellar luminosity in the u band. In the figure, the total time span between the first and last epoch of cluster observation is shown as the gray region.

## 6. Summary and Discussion

We have conducted a pilot study to search for IMBHs in dense stellar systems, one that uses TDEs as a probe of the presence of  $10^3\,M_\odot \lesssim M_\bullet \lesssim 10^5\,M_\odot$  black holes embedded in stellar cusps at the center of massive GCs. Following previous work, we have modeled the long super-Eddington accretion phase in the slim advective disk regime together with the accompanying adiabatically expanding radiation-driven outflow. The ensuing optical/UV flare easily outshines the brightness of the (old) stellar population of GCs for a period of months to years, making TDEs triggered by IMBHs in principle detectable in a large sample of GCs. The disruption rate of main-sequence stars as a function of black hole mass and GC properties was estimated with a simple model of losscone dynamics and the help of a numerical 1D Fokker–Planck approach.

Large surveys with precise multiwavelength photometry are becoming increasingly available for public use. As an illustrative example, we have taken advantage of the NGVS, an optical near-infrared imaging survey of the Virgo galaxy

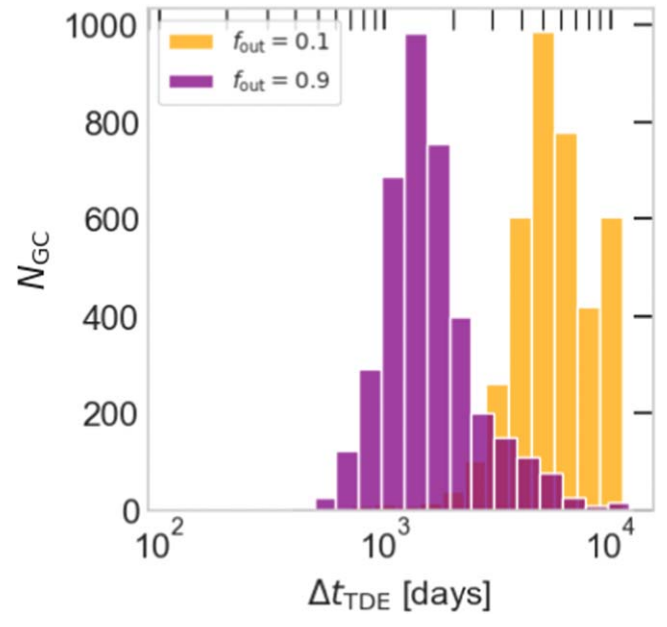


**Figure 8.** Distribution of  $\Delta t_{\rm TDE}$  timescales (see the main text for details) for our sample of GCs at varying  $f_{\rm out}$ , with the weaker winds+disk systems outshining the steady stellar component for longer timescales because of late time accretion.

cluster, and of its robust sample of GCs observed in the u and g bands. We have checked for the presence of large photometric variations in the u band induced by potential TDE flares and found no obvious candidates. Since our model predicts as many as  $10 \times f_{\rm occ}$  detectable events in the NGVS sample, the lack of recognizable candidates in the data implies that the fraction of GCs harboring IMBHs must be  $f_{\rm occ} \lesssim 10\%$ . This is not very constraining, as postmerger recoil kicks originated by anisotropic GW emission may make it hard for IMBHs to be retained in lower-dispersion parent clusters (e.g., Arca Sedda et al. 2023).

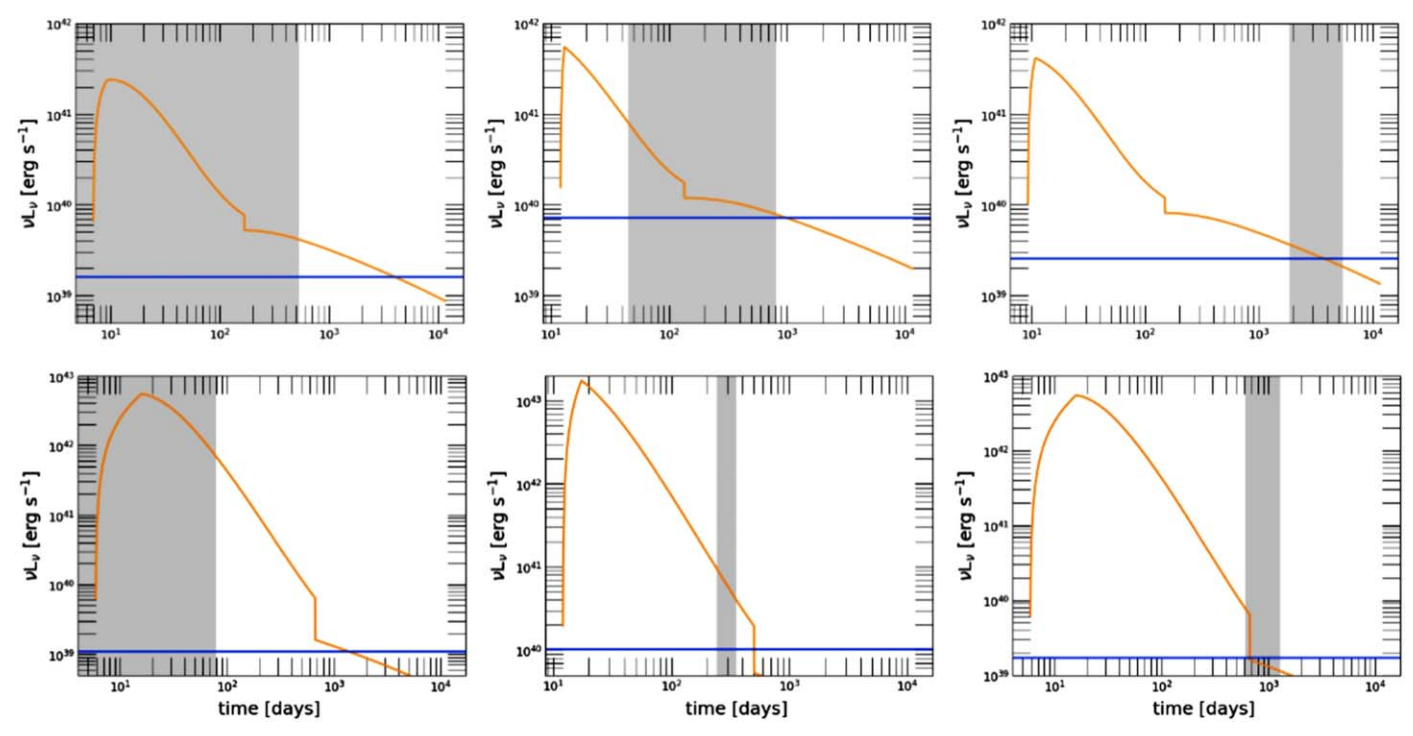


Figure 9. Three examples of TDE detections from our Monte Carlo simulations. Each light curve is computed in the u band (solid orange line) for  $f_{\rm out}=0.1$  (top panel) and  $f_{\rm out}=0.9$  (bottom panel) with IMBH mass  $M_{\bullet}=0.01~M_{\rm GC}$ . The solid blue line shows the GC mean monochromatic luminosity while the gray shaded region marks the total time span between the first and last epoch of cluster observation,  $\Delta t_S$  (see the main text for details). From top left to bottom right, the masses of the IMBHs responsible for the TDE are  $1.39 \times 10^4$ ,  $1.26 \times 10^5$ ,  $9.25 \times 10^4$ ,  $3.02 \times 10^4$ ,  $1.26 \times 10^5$ , and  $3.03 \times 10^4 M_{\odot}$ .

Naturally, better modeling of the properties of the cluster central stellar distribution and of TDE light curves and rates are all needed to gain deeper insights into the presence of IMBHs in GCs. Large samples of extragalactic star clusters, like those that will be assembled by the Vera C. Rubin Observatory (Usher et al. 2023), should enable significant progress in the search for TDEs in dense stellar systems. While there are considerable uncertainties in the modeling of TDE events in GCs, we hope that our pilot investigation will provide a blueprint for future searches of optical flares triggered by IMBHs.

## Acknowledgments

Support for this work was provided by NASA through grants 80NSSC21K027 and 80NSSC22K0814 (P.M.) and by a Eugene-Cota Robles Fellowship to V.T. E.B. acknowledges support from the European Research Council (ERC) under the European Union's Horizon 2020 research and innovation program ERC-2018-CoG under grant agreement 818691 (B Massive), from the European Consortium for Astroparticle Theory in the form of an Exchange Travel Grant, and the European Union's Horizon 2020 Programme under the AHEAD2020 project (grant agreement 871158). We acknowledge useful discussions on this project with G. Lodato and E. Rossi.

# ORCID iDs

Piero Madau https://orcid.org/0000-0002-6336-3293 Elisa Bortolas https://orcid.org/0000-0001-9458-821X

#### References

```
Alexander, T., & Hopman, C. 2009, ApJ, 697, 1861Arca Sedda, M., Kamlah, A. W. H., Spurzem, R., et al. 2023, MNRAS, 526, 429
```

```
Bahcall, J. N., & Wolf, R. A. 1977, ApJ, 216, 883
Baumgardt, H., He, C., Sweet, S. M., et al. 2019, MNRAS, 488, 5340
Baumgardt, H., & Hilker, M. 2018, MNRAS, 478, 1520
Baumgardt, H., Makino, J., & Ebisuzaki, T. 2004, ApJ, 613, 1133
Binney, J., & Tremaine, S. 1987, Galactic Dynamics (Princeton, NJ: Princeton
   Univ. Press)
Bortolas, E. 2022, MNRAS, 511, 2885
Bovy, J., Hogg, D. W., & Roweis, S. T. 2011, AnApS, 5, 1657
Chen, J.-H., & Shen, R.-F. 2018, ApJ, 867, 20
Coughlin, E. R., & Begelman, M. C. 2014, ApJ, 781, 82
Coughlin, E. R., & Nixon, C. J. 2019, ApJL, 883, L17
Dotan, C., & Shaviv, N. J. 2011, MNRAS, 413, 1623
Evans, C. R., & Kochanek, C. S. 1989, ApJL, 346, L13
Feldmeier, A., Lützgendorf, N., Neumayer, N., et al. 2013, A&A, 554, A63
Ferrarese, L., Côté, P., Cuillandre, J.-C., et al. 2012, ApJS, 200, 4
Fragione, G., Ginsburg, I., & Kocsis, B. 2018a, ApJ, 856, 92
Fragione, G., Leigh, N. W. C., Ginsburg, I., & Kocsis, B. 2018b, ApJ, 867, 119
Frank, J., & Rees, M. J. 1976, MNRAS, 176, 633
Giersz, M., Leigh, N., Hypki, A., Lützgendorf, N., & Askar, A. 2015,
Greene, J. E., Strader, J., & Ho, L. C. 2020, ARA&A, 58, 257
Guillochon, J., & Ramirez-Ruiz, E. 2013, ApJ, 767, 25
Holley-Bockelmann, K., Gültekin, K., Shoemaker, D., & Yunes, N. 2008, ApJ,
Ibata, R., Bellazzini, M., Chapman, S. C., et al. 2009, ApJL, 699, L169
Jordán, A., McLaughlin, D. E., Côté, P., et al. 2007, ApJS, 171, 101
Kamann, S., Husser, T. O., Brinchmann, J., et al. 2016, A&A, 588, A149
Kippenhahn, R., & Weigert, A. 1990, Stellar Structure and Evolution (Berlin:
   Springer)
Kitaki, T., Mineshige, S., Ohsuga, K., & Kawashima, T. 2021, PASJ, 73, 450
Kochanek, C. S. 2016, MNRAS, 461, 371
Law-Smith, J. A. P., Coulter, D. A., Guillochon, J., Mockler, B., &
   Ramirez-Ruiz, E. 2020, ApJ, 905, 141
Lightman, A. P., & Shapiro, S. L. 1977, ApJ, 211, 244
Lin, D., Strader, J., Carrasco, E. R., et al. 2018, NatAs, 2, 656
Lodato, G., King, A. R., & Pringle, J. E. 2009, MNRAS, 392, 332
Lodato, G., & Rossi, E. M. 2011, MNRAS, 410, 359
Lu, W., & Bonnerot, C. 2020, MNRAS, 492, 686
Lützgendorf, N., Kissler-Patig, M., Neumayer, N., et al. 2013, A&A, 555, A26
Magorrian, J., & Tremaine, S. 1999, MNRAS, 309, 447
Mei, S., Blakeslee, J. P., Cote, P., et al. 2007, ApJ, 655, 144
```

```
Merritt, D. 2004, in Coevolution of Black Holes and Galaxies, ed. L. C. Ho (Cambridge: Cambridge Univ. Press), 263

Metzger, B. D., & Stone, N. C. 2016, MNRAS, 461, 948

Miller, M. C., & Davies, M. B. 2012, ApJ, 755, 81

Miller, M. C., & Hamilton, D. P. 2002, MNRAS, 330, 232

Mockler, B., Guillochon, J., & Ramirez-Ruiz, E. 2019, ApJ, 872, 151

Muñoz, R. P., Puzia, T. H., Lançon, A., et al. 2014, ApJS, 210, 4

Nguyen, D. D., Seth, A. C., Neumayer, N., et al. 2019, ApJ, 872, 104

Ohsuga, K., Mori, M., Nakamoto, T., & Mineshige, S. 2005, ApJ, 628, 368

Portegies Zwart, S. F., & McMillan, S. L. W. 2002, ApJ, 576, 899

Ramirez-Ruiz, E., & Rosswog, S. 2009, ApJL, 697, L77

Rees, M. J. 1988, Natur, 333, 523

Rossi, E. M., Stone, N. C., Law-Smith, J. A. P., et al. 2021, SSRv, 217, 40

Roth, N., Rossi, E. M., Krolik, J., et al. 2020, SSRv, 216, 114

Ryu, T., Krolik, J., & Piran, T. 2020, ApJ, 904, 73
```

```
Spitzer, L. 1987, Dynamical Evolution of Globular Clusters (Princeton, NJ:
  Princeton Univ. Press)
Stone, N. C., & Metzger, B. D. 2016, MNRAS, 455, 859
Strubbe, L. E., & Quataert, E. 2009, MNRAS, 400, 2070
Strubbe, L. E., & Quataert, E. 2011, MNRAS, 415, 168
Syer, D., & Ulmer, A. 1999, MNRAS, 306, 35
Tremou, E., Strader, J., Chomiuk, L., et al. 2018, ApJ, 862, 16
Usher, C., Dage, K. C., Girardi, L., et al. 2023, PASP, 135, 074201
Vasiliev, E. 2017, ApJ, 848, 10
Vitral, E., & Mamon, G. A. 2021, A&A, 646, A63
Wang, J., & Merritt, D. 2004, ApJ, 600, 149
Webb, N., Cseh, D., Lenc, E., et al. 2012, Sci, 337, 554
Wen, S., Jonker, P. G., Stone, N. C., & Zabludoff, A. I. 2021, ApJ, 918, 46
Wu, S., Coughlin, E. R., & Nixon, C. 2018, MNRAS, 478, 3016
Zhao, H. 1996, MNRAS, 278, 488
Zocchi, A., Gieles, M., & Hénault-Brunet, V. 2019, MNRAS, 482, 4713
```